Chinese Chemical Letters 36 (2025) 110015

Contents lists available at ScienceDirect

Chinese Chemical Letters

journal homepage: www.elsevier.com/locate/cclet

P2-type low-cost and moisture-stable cathode for sodium-ion batteries

Xuan Wang[a,1], Peng Sun[a,1], Siteng Yuan[a], Lu Yue[a,*], Yufeng Zhao[b,*]

[a] Key Laboratory for Advanced Technology in Environmental Protection of Jiangsu Province, Yancheng Institute of Technology, Yancheng 224051, China
[b] Institute for Sustainable Energy & College of Sciences, Shanghai University, Shanghai 200444, China

ARTICLE INFO

Article history:
Received 1 April 2024
Revised 24 April 2024
Accepted 14 May 2024
Available online 15 May 2024

Keywords:
Cathode material
P2 phase
Moisture sensitivity
Low-cost
Sodium-ion batteries

ABSTRACT

Mn-based P2-type oxides are considered as promising cathodes for Na-ion batteries; however, they face significant challenges, including structural degradation when charged at high cutoff voltages and structural changes upon storing in a humid atmosphere. In response to these issues, we have designed an oxide with co-doping of Cu and Al which can balance both cost and structural stability. The redox reaction of $Cu^{2+/3+}$ can provide certain charge compensation, and the introduction of Al can further suppress the Jahn-Teller effect of Mn, thereby achieving superior long-term cycling performance. The *ex-situ* XRD testing indicates that Cu/Al co-doping can effectively suppress the phase transition of P2-O2 at high voltage, thereby explaining the improvement in electrochemical performance. DFT calculations reveal a high chemical tolerance to moisture, with lower adsorption energy for H_2O compared to pure $Na_{0.67}Cu_{0.25}Mn_{0.75}O_2$. A representative $Na_{0.67}Cu_{0.20}Al_{0.05}Mn_{0.75}O_2$ cathode demonstrates impressive reversible capacities of 148.7 mAh/g at 0.2 C, along with a remarkable capacity retention of 79.1% (2 C, 500 cycles).

© 2025 Published by Elsevier B.V. on behalf of Chinese Chemical Society and Institute of Materia Medica, Chinese Academy of Medical Sciences.

The escalating consumption of non-renewable resources like coal and oil has intensified concerns about resource scarcity and environmental pollution [1]. In response, there is a growing imperative to reduce reliance on fossil energy, leading to the ascendancy of new energy vehicles equipped with lithium-ion batteries (LIBs) as the prevailing mode of transportation [2,3]. However, the overutilization of LIBs in grid-scale storage has been limited by the relatively low abundance of Li resources in earth's crust and its uneven distribution [4,5]. As a globally abundant element (the sixth abundant element on earth), sodium is a good substitute for lithium. Meanwhile, the reaction mechanism of sodium-ion batteries (SIBs) is similar to that of LIBs, and the standard hydrogen potential of Na^+ is −2.71 V which is very close to that of Li^+ (−3.04 V) [6]. This suggests that sodium-ion batteries hold considerable potential to supplant lithium-ion batteries in the energy storage sector in the future [7,8]. Based on this, the reported cathode material for sodium-ion batteries mainly include oxide, polyanion, prussian blue analogues, among which, the layered oxide cathode material is the main cathode material for sodium-ion batteries due to the advantages of simple preparation method, high specific capacity and voltage. Based on the coordination configuration of Na^+ in MO_6 polyhedral and the stacking pattern of O^{2-}, the layered oxides mainly divide into two structures, such as P2 and O3 phase [9]. P2-phase layered materials have attracted more attention because of their larger layer spacing and faster sodium ion transport rates. Currently, the main cathode material used for sodium-ion batteries cathode are P2-phase Ni/Mn based material, *i.e.*, $Na_{0.67}Ni_{0.33}Mn_{0.67}O_2$ can release a high capacity of 160 mAh/g in the voltage range of 2.0–4.5 V [10]. However, there are some problems associated with these P2 materials, including transition metal (TMO_2) slippage at high charge plateaus due to the Na^+/vacancy ordering [11]. In order to solve the phase transition problems, the incorporation of metallic element such as Co, Mg, Zn, and Ti are common modification method [12–15]. However, these cathode materials are mainly based on $Ni^{2+/3+/4+}$redox couples to realize charge compensation. Nevertheless, highly reactive Ni^{4+} ions may react with the electrolyte, which would critically affect the degradation of the cathode materials [16]. Furthermore, the widespread utilization of nickel (Ni) in lithium-ion materials has led to a significant surge in the global price of nickel resources. Currently, sodium-ion batteries primarily target the realm of large-scale energy storage, necessitating more stringent control over the cost of source materials. Cu is one of the most abundant resources on the earth, unlike in the lithium layered oxides, copper is reported to have redox activity in Na_xTMO_2 [17]. Hu *et al.* [18] developed P2-type $Na_{0.67}Cu_{0.33}Mn_{0.67}O_2$ composite, which can deliver a specific capacity of 70 mAh/g between 2.5–4.2 V which

* Corresponding authors.
E-mail addresses: Yuelu66@126.com (L. Yue), yufengzhao@shu.edu.cn (Y. Zhao).
[1] These authors contributed equally to this work.

https://doi.org/10.1016/j.cclet.2024.110015
1001-8417/© 2025 Published by Elsevier B.V. on behalf of Chinese Chemical Society and Institute of Materia Medica, Chinese Academy of Medical Sciences.

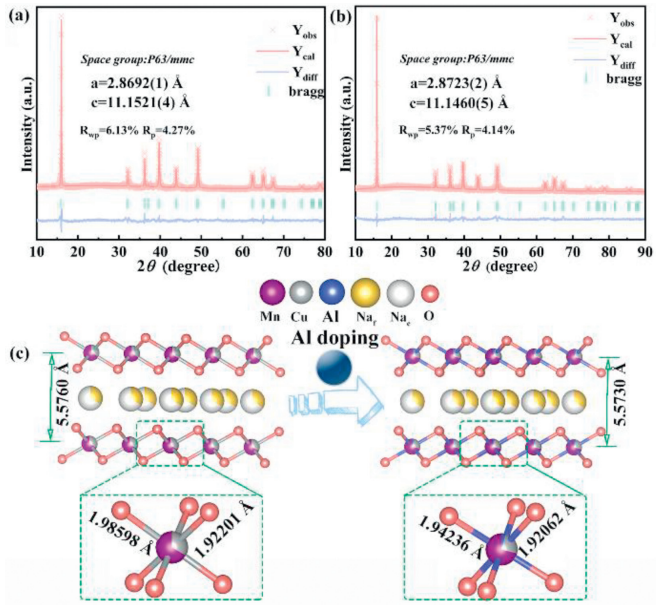

Fig. 1. X-ray diffraction pattern and Rietveld refinement of (a) NCM and (b) NCAM. (c) Schematic illustration of effect of Al^{3+} doping on electrode structure.

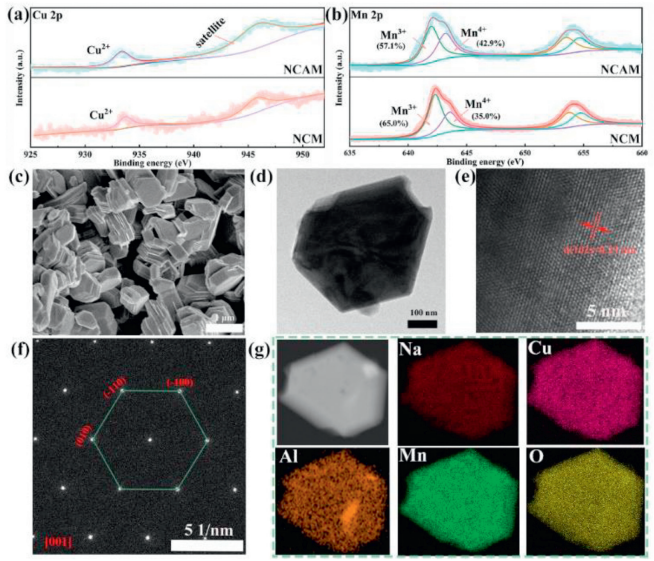

Fig. 2. XPS spectra comparison of (a) Cu 2p and (b) Mn 2p. (c) FESEM, (d, e) HRTEM analysis, (f) SAED pattern and (g) EDS mapping results of NCAM.

mainly based on $Cu^{2+/3+}$ redox reaction. Evidently, the capacity of 70 mAh/g falls short of meeting the energy storage requirements for sodium-ion batteries. Beyond the electrochemical performance challenges stemming from structural transitions, the moisture sensitivity emerges as a crucial factor for practical applications. This concern is particularly significant due to the expansive interlayer spacing of P2-type cathode material, facilitating the easy insertion of water molecules [19]. Therefore, exploring a P2 phase material that can balance cost, electrochemical performance and moisture sensitivity is of great significance.

Herein, we proposed a ternary P2 phase cathode material based on Cu-Al-Mn elements for sodium-ion batteries via solvothermal method combined with solid reaction process. The low-cost Cu elements mainly provide charge compensation in high voltage regions, the incorporation of Al can stabilize the structure of P2 phase materials to a certain extent when Mn ions participated in redox reaction, leading to a better phase reversibility and long cycle life. Consequently, the prepared $Na_{0.67}Cu_{0.20}Al_{0.05}Mn_{0.75}O_2$ demonstrates improved electrochemical performance with a decent capacity of 148.7 mAh/g at 0.2 C and capacity retention of 79.1% over 500 cycles. Notably, Density functional theory (DFT) calculation results reveal that the adsorption energy of the H_2O molecule is less than the sample without Al-doping, meaning a better moisture sensitivity. As observed in this study, the strategy provides valuable guidelines for the rational control of SIB performance and to achieve further application in the field of energy storage.

To ascertain the crystal structures of the synthesized materials $Na_{0.67}Cu_{0.20}Al_{0.05}Mn_{0.75}O_2$ (NCAM) and $Na_{0.67}Cu_{0.25}Mn_{0.75}O_2$ (NCM), X-ray diffraction (XRD) tests were conducted on both samples, and the corresponding Rietveld refinement patterns are depicted in Figs. 1a and b. The results reveal that all diffraction peaks of the synthesized NCM and NCAM cathode materials exhibit P2-type stacking sequence, indicative of P_{63}/mmc symmetry [20]. Notably, the incorporation of Al does not result in the emergence of any new diffraction peaks, signifying effective incorporation of Al into the layered cathode material lattice. The refined crystallographic parameters for NCAM and NCM can be found in Tables S1 and S2 (Supporting information). Within the P2-type layered cathode material, the transition metal occupies the center of the MO_6 octahedron, while sodium assumes the trigonal position. In P2-type layered cathode materials, the transition metal assumes a central position within the MO_6 octahedron, while sodium occupies the trigonal position. This crystallographic arrangement signifies a critical structural characteristic in the layered cathode material [21]. Upon scrutinizing the refined structural parameters of non-doped cathode material (NCM), it becomes evident that aluminum (Al) ions strategically occupy the center of the octahedron at the Wycoff 2a position. Simultaneously, oxygen atoms are positioned at the Wycoff 4f position within the crystal lattice [22]. Considering the ionic radius of Al^{3+} is (0.55 Å) is very close to the ionic radius of Mn^{4+} (0.54 Å), it proximity suggests a plausible scenario wherein Al effectively replaces a portion of the Mn^{4+} ions during the doping process, contributing to the structural modifications observed in the layered cathode material [23,24]. The structures of NCAM and NCM are depicted in Fig. 1c, the lengths of Mn-O bonds and spacings of c-axis are calculated from the refinements results (Tables S1 and S2). Significantly, in the un-doped oxide (NCM) sample, there is a more pronounced variation in the bond length of Mn-O bond, ranging from a minimum of 1.9220 Å to a maximum of 1.9859 Å. In contrast, the Al-doped counterpart (NCAM) exhibits a notably reduced distortion in the P2-$Na_{0.67}Cu_{0.20}Al_{0.05}Mn_{0.75}O_2$ phase. The Mn-O bond length in NCAM show a smaller range, with the shortest distance measuring 1.9206 Å and the longest being 1.9423 Å. In Mn-based cathode material, the high-spin Mn^{3+} with the electron configuration of $(t_{2g})^3(e_g)^1$ in the 3d orbital usually produces a Jahn-teller distortion. This geometric distortion with two longer and the other two shorter Mn-O axial bonds (other than the equatorial Mn-bonds in structure without distortion), usually reduces the symmetry and energy of nonlinear molecular system, and leads to a structural disorder and a strong strain in the structure [25]. Therefore, in this work, it can be considered Al-doping would lead to the destructive Jahn-Teller effect, thereby reducing the structural distortion of the layered oxide and improving the cycle stability [26].

The composition and chemical state information of the NCAM and NCM were investigated by XPS (Fig. S1 in Supporting information). No extra peaks other than Na, Al, Cu, Mn, O can be detected, suggesting the high purity of both samples. Specifically, Fig. 2a shows the high-resolution Cu 2p core-level XPS spectra of the two samples, from which the valence of Cu in NCAM and NCM

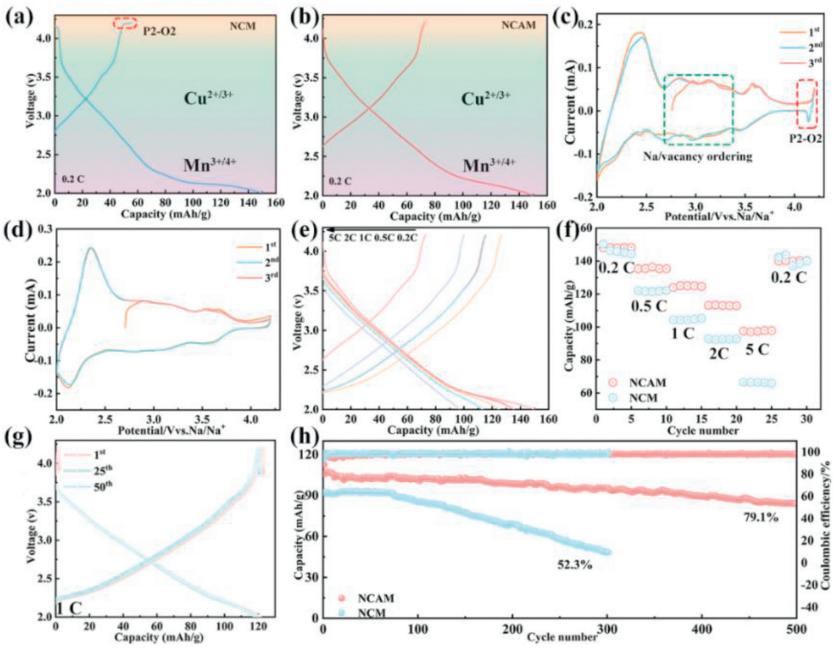

Fig. 3. Galvanostatic charge/discharge curve of (a) NCM and (b) NCAM at a current rate of 0.2 C for the first cycle. d*Q*/d*V* plots of (c) NCM and (d) NCAM. (e) Voltage curves of NCAM cycled at different C-rates between 2.0 V and 4.2 V. (f) Rate capability comparison two samples. (g) Galvanostatic charge/discharge curves of NCAM at 1 C for 50 cycles. (h) Long cycle stability comparison of NCM and NCAM.

can be indexed to divalent [27]. The high-resolution spectrum of Al 2p (Fig. S2 in Supporting information) in NCAM which representing the effective doping of Al and the peak at 74.2 eV indicate the tetravalent state of Al [28]. Fig. 2b shows that the Mn in both samples are at a mixture of trivalent and tetravalent [29]. It can be found that the content of trivalent manganese in the NCM is higher than that of the NCAM electrode, so that more $Mn^{3+/4+}$ redox reactions would involve in charge compensation capacity in the low-voltage region which are detrimental to the stability of the layered structure [26].

The morphological feature and particle size of NNCM were also investigated by field emission scanning electron microscope (FESEM) and high-resolution transmission electron microscope (HRTEM). Fig. 2c (NCAM) and Fig. S3a (Supporting information, NCM) reveals a hexagonal sheet-like morphology for both materials, with the NCAM cathode material exhibiting a more regular hexagonal structure and a more uniform distribution of particles. Notably, the introduction of Al^{3+} during the doping process results in a reduction in particle size, a characteristic observed in Fig S3b (Supporting information). This reduction is anticipated to enhance the material's sodium-ion migration kinetics, thereby contributing to the overall performance enhancement of the NCAM cathode material [30]. Fig. 2d further demonstrates that NCAM presents as a hexagonal-like shape in the TEM image. HRTEM analysis suggests clear lattice fringes with inter planar spacing of 2.3 Å for NCAM (Fig. 2e), which can be ascribed to the (102) planes of the typical P2-type layered structure. The corresponding selected area electron diffraction (SAED) pattern in Fig. 2f confirms that the sample $Na_{0.67}Cu_{0.20}Al_{0.05}Mn_{0.75}O_2$ possesses a single crystal hexagonal structure. Besides, the EDS mapping in Fig. 2g reveals uniform distribution of all elements on the interior of the samples.

The various electrochemical tests of NCAM and NCM electrodes were tested in Na half-cell system at room temperature (1 C = 150 mA/g). Figs. 3a and b display the first cycle charge-discharge curves for NCAM and NCM, respectively. Two samples can release specific capacities of 148.7 mAh/g (NCAM) and 149.5 mAh/g (NCM) at 0.2 C in the voltage range of 2.0–4.2 V, respectively, and there is only a tiny difference in capacity at small current density. Accordingly, the capacity at high voltage (light green region) comes from the redox reaction of $Cu^{2+/3+}$, while the light red region marked in Figs. 3a and b are assigned to the $Mn^{3+/4+}$ redox reaction [18,31]. It can be assumed that the capacities of both electrode materials are provided by the $Mn^{3+/4+}$ and $Cu^{2+/3+}$ redox reactions. It should be emphasized here that the incorporated Al in NCAM samples does not participate in charge compensation and only serves to stabilize the crystal structure [32,33]. In addition, a short plateau appears at the end of the charge curve of the NCM electrode material when it is charged to high voltage, indicating the phase transition from P2 to O2 [34]. The P2 phase cathode materials always undergoes a P2-O2 phase transition in the high-voltage state, which is accompanied by a large volume contraction (~23%). The large volume change reduces the electronic conductivity and structural stability of the electrode material, leading to a serious degradation of the cycling performance of the material [35]. In contrast, the charge/discharge curve of NCAM electrode is relatively smooth, suggesting that the Al doping could effectively suppress the P2-O2 phase transition, ensuring better structural stability during charging and discharging [36,37]. The difference between the charge/discharge curves of the two samples is more evident in the cyclic voltammetry (CV) curves (Figs. 3c and d). More specifically, the NCM electrode shows a pair of redox peaks around about 4.1 V, representing the occurrence of P2-O2 phase transition, which is consistent with the charge-discharge curve at high potential (Fig. 3c). Furthermore, some undesired tiny peaks appears on the CV curves of the NCM electrode which cannot be attributed to any redox reaction, it is generally believed that these tiny peaks are related to the Na/vacancy ordering, which would deteriorate the diffusion kinetics of Na^+ [38,39]. However, the CV curves of the NCAM electrode is much smoother compared to the NCM, representing an effective restraining of the Na/vacancy ordering. The redox peaks below 2.5 V for both NCAM and NCM electrode can be indexed to the redox reaction of $Mn^{3+/4+}$ [40]. Moreover, the redox peaks at 3.65/3.53 V for both samples can be considered to be caused by the redox reaction of $Cu^{2+/3+}$ [18]. More importantly, the overlapping of the CV curves (NCAM) is significantly better than that of NCM, indicating its better reversibility

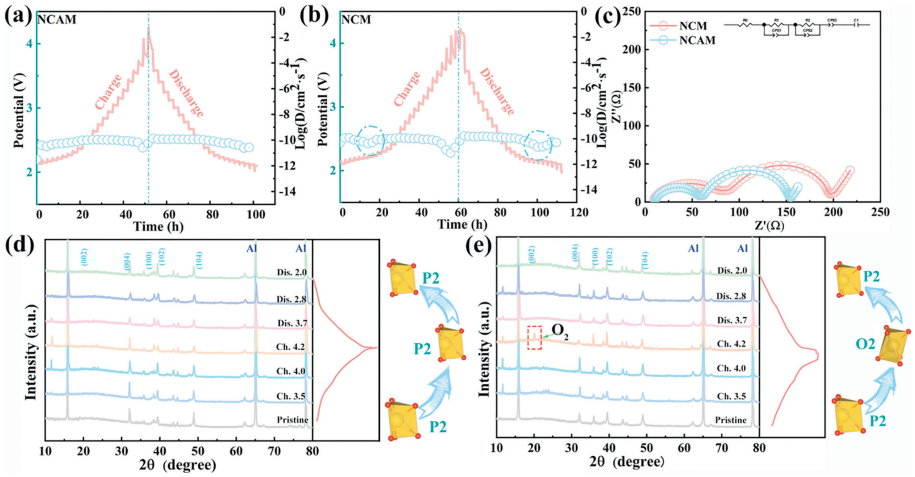

Fig. 4. GITT curves and corresponding sodium-ion diffusion coefficients D_{Na^+} of (a) NCAM and (b) NCM. (c) Nyquist plots comparison of the initial electrodes. *Ex-situ* XRD pattern of (d) NCAM and (e) NCM.

of redox reaction [41]. To further reveal the merits of NCAM, the rate performance tests were conducted. As shown in Fig. 3e, the NCAM cathode material could yield a discharge capacity of 148.7, 135.3, 125.0, 113.3 and 97.0 mAh/g at 0.2, 0.5, 1, 2 and 5 C, respectively. However, for sample NCM, it can only deliver a specific capacity of 65.7 mAh/g at 5 C (Fig. S4b in Supporting information). The differences in electrochemical performance electrochemical can be more intuitively illustrated in the rate capability of the samples (Fig. 3f). Furthermore, the comparison of galvanostatic charge/discharge curves for NCAM and NCM at 1 C for the first 50 cycles are displayed in Fig. 3g and Fig. S5 (Supporting information), from which it can be found that the NCAM electrode demonstrates a better electrochemical reversibility and capacity retention (Fig. 3g). Comparatively, the NCM electrode shows relatively inferior rate performance than NCAM (Fig. S5). Above all, benefit from the effective suppression of the phase transition and Na/vacancy ordering, the NCAM electrodes exhibit superior long-cycle performance with a high capacity retention of 79.1% at 2 C after 500 cycles which is obvious superior than that of NCM (52.3% at 2 C after 300 cycles) (Fig. 3h).

To better understand the underlining reason for the enhanced performance, the Na^+ transport kinetics within the cathode material was examined by testing the Na^+ diffusion coefficients of NCM and NCAM through galvanostatic intermittent titration technique (GITT) and electrochemical impedance spectroscopy (EIS) techniques [42]. The specific definition of GITT can be found in supporting information. As shown in Figs. 4a and b, generally, the diffusion coefficient of Na^+ for both samples are in the same order of magnitude, *i.e.*, 10^{-11}–10^{-10}. Nevertheless, the fluctuation of diffusion coefficient of NCAM is smaller during the charge/discharge process. Importantly, an obvious fluctuation in the diffusion coefficient of Na^+ corresponding to the $Mn^{3+/4+}$ redox reaction can be observed in NCM electrode, indicating the incorporation of Al in the structure enables to suppress the Jahn-Teller distortion of Mn^{3+} which may result in more smooth electrochemistry of the NCAM than that of the NCM [43,44]. In addition, the Na^+ diffusion coefficient of NCM shows a more serious decline at the end of charging process (above 3.8 V) when compared with NCAM. Such a decline could be attributed to a phase transition, which further confirms that the incorporation can efficiently suppress the P2-O2 phase transition [45]. EIS was applied on the initial electrode and the cell charged/discharged at 1 C after 100 cycles. Fig. 4c and Fig. S6 (Supporting information) show the comparison of Nyquist plots before and after cycling of the two electrodes, respectively. In Fig. 4c, the Nyquist plots reveal the presence of two semicircles corresponding to sodium ions' extraction/insertion reactions into the cathode material. The semicircle observed in the high-frequency region signifies the resistance associated with the surface or solid electrolyte interphase (SEI) layer. On the other hand, the semicircle at low frequency is indicative of the charge transfer resistance (R_{ct}) linked to the extraction and insertion of sodium ions [46,47]. The R_{ct} values for the initial NCAM and NCM electrodes are 87 Ω and 115 Ω, respectively. It turns out that Al-doping can effectively reduce the charge transfer resistance of sodium ion intercalation/deintercalation, which also explains its better rate capability of NCAM than NCM. Furthermore, the R_{ct} values of NCAM and NCM both increase after 100 cycles (Fig. S6). However, the increased resistance of NCAM is much less than that of NCM, demonstrating that the introduction of Al can improve the structural stability of the P2 phase after multiple charge and discharge cycles [48].

In order to gain more insight into the Na intercalation/deintercalation mechanism and more specifically on the effect of the Al substitution on the Na-driven crystal structure transition, *ex-situ* XRD measurement was conducted during the initial charge/discharge process at 0.1 C in the voltage range of 2.0–4.2 V (Figs. 4d and e). For the NCM electrode, when it was charged to 4.2 V, the typical (004), (100) and (102) characteristic peaks of the P2 phase weaken significantly, while a new O2 type (002′) diffraction peak appears at 20°, indicating that the NCM electrode does undergo a P2-O2 phase transition at high voltage, which is consistent with the previous charge/discharge curves and CV analysis [49]. In P2 type cathode material, the Na atoms occupy trigonal prismatic sites between neighboring oxygen planes. When the Na is removed, the central MO_2 sheet glides in the a-b plane to avoid close oxygen-oxygen contacts. However, there are two choices for the slide direction that place the neighboring O atom planes in a close-packed configuration. Stacking faults occur because these two choices are selected at random, which would finally leading to the phases transition [10]. It is generally considered the P2-O2 phase transition is associated with the rapid capacity fade [50]. In contrast, for Al substituted sample, *ex-situ* XRD patterns taken after charging to 4.2 V (Fig. 4e) shows no sign of phase transition. All the major diffraction peaks corresponding to the P2 phase were clearly maintained for the NCAM sample with Al-doping. Accordingly, the *ex-situ* XRD results strongly suggest that the incorporation of Al can effectively improves the P2-type structural stability, thus leading to a better electrochemical performance.

In addition, the moisture sensitivity is a non-negligible factor for practical applications. As to practical application, most of the Na-M-O cathode materials are hygroscopic, which would react

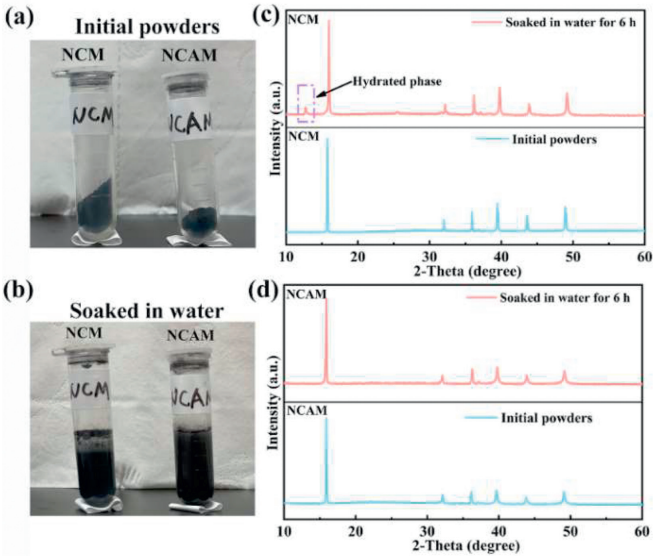

Fig. 5. (a) The initial materials of NCAM and NCM. (b) NCM and NCAM material soaked in water. (c) XRD comparison between NCM initial material and immersion in water for 6 h. (d) XRD comparison between NCAM initial material and immersion in water for 6 h.

with water in the air to form hydrated phase, thus increasing the material storage cost [51,52]. To test the moisture stability of synthetized cathode materials, the as-prepared cathode powders were directly exposed to air for 6 h and then soaked in water for 6 h, followed by drying at 90 °C for 12 h in vacuum oven (Figs. 5a and b). The XRD results of the two electrode materials before and after water immersion are compared (Figs. 5c and d). The NCM sample without Al doping showed an obvious diffraction peak at 12.5° after soaking in water for 6 h, which can be attributed to the hydrate phase (Fig. 5c) [53]. This means that water molecules can easily enter into the NCM electrode material, indicating a worse moisture stability. In contrast, the XRD diffraction peak of NCAM electrode material after soaking in water are almost no different from the structure of the initial powder, meaning the NCAM electrode can keep a better structural stability in a humid environment (Fig. 5d).

From the previous refinement results, it can be found that with the incorporation of Al, the *c*-axis length of NCAM electrode becomes shorter, implying that the sodium layer spacing becomes smaller [54]. Therefore, it is inferred that the smaller sodium layer spacing hinders the entry of water molecules to a certain extent [55,56]. Furthermore, the adsorption energy of the H_2O molecule (referred to as $\Delta E_{ads,}$ the specific definition of ΔE_{ads} can be seen in Support Information) is also related to the moisture stability of layered oxides [57,58]. In order to determine the moisture stability of the two cathode materials, DFT calculations were carried out. H_2O molecules were set to located in the sodium layer to find the model with the lowest total energy. As shown in Figs. 6a and b, the calculated ΔE_{ads} value of NCM (−2.98 eV) is smaller than that of NCAM (−1.35 eV), indicating H_2O molecules are more likely to enter the sodium interlayer of the sample NCM. Therefore, the incorporation of Al can be effective in improving the moisture stability of the NCAM, which is an advantage for the practical application. The water-soaked materials after drying were further assembled into half-cells and tested again for their electrochemical properties. The charge/discharge profiles are displayed in Figs. 6c and d. The NCAM cathode delivers discharge capacities of 137.2 mAh/g (0.2 C), 110.8 mAh/g (0.5 C), 98.9 mAh/g (1 C), 84.2 mAh/g (2 C), and 70.2 mAh/g (5 C), respectively (Fig. 6c). Even at 5 C, the water-soaked cathode material can still maintain a decent capacity close to that of the original material. In contrast, the water-soaked NCM cathode only exhibits 45.1 mAh/g at 2 C (Fig. 6d), indicating soaking in water has a significant negative effect on the structure of the material. We also tested the long-term cycling performance of electrode materials after soaking in water at 0.5 C, as shown in Fig. S7 (Supporting information). The NCAM electrode can still maintain a capacity retention rate of 75.1% after 500 cycles which is superior than NCM. It should be mentioned that NCM electrodes often crashed during the testing process which may be related to the instability of the NCM structure after soaking in water. Moreover, GITT was also conducted on the water-soaked electrode. As shown in Fig. 6f, the diffusion coefficient of Na^+ for NCM shows an obvious decline with the order of 10^{-12} which is obvious lower than the initial NCM electrode (Fig. 4b). This demonstrates the great impediment to sodium ion transport caused by the entry of water molecules into the sodium layer. The sodium ion diffusion coefficient of NCAM was not significantly different from the initial electrode (Fig. 6e), which can still be maintained to be close to the order of 10^{-10}. In addition, EIS tests were conducted on both electrode materials after soaking in water (Fig. S8 in Supporting information). It can be found that the R_{ct} of NCM electrode significantly increased. This is mainly because water molecules enter the sodium layer, which will have an adverse effect on the

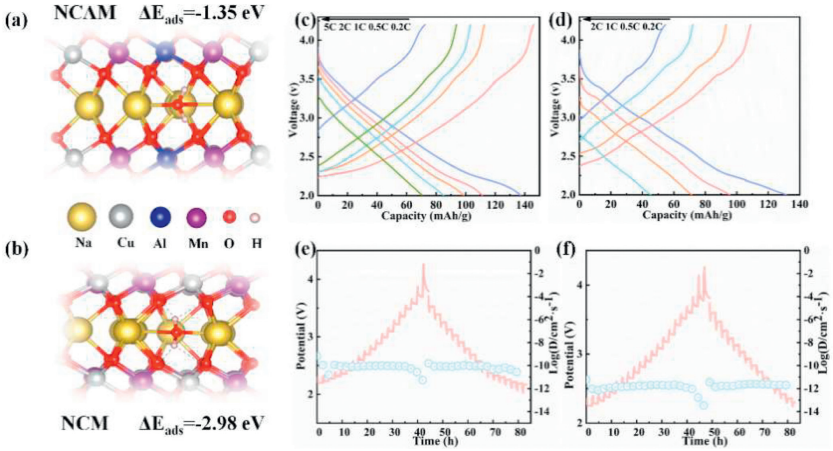

Fig. 6. DFT-calculated ΔE_{ads} for moisture-exposed (a) NCAM and (b) NCM. Rate performance of (c) NCAM and (d) NCM between 2.0 V and 4.2 V after soaking in water. GITT curves and corresponding sodium-ion diffusion coefficients D_{Na^+} of (e) NCAM and (f) NCM after soaking in water.

de-intercalation of sodium ions, leading to an increase in charge transfer impedance. All these analyses show that Al doping is beneficial in enhancing the moisture stability of P2 type material and the good stability of NCAM in humid air which can facilitates its storage as a large-scale energy storage material for sodium-ion batteries.

In this work, a low-cost P2-phase cathode material for sodium-ion batteries has been synthesized by solvothermal method. The strategy eliminates the use of expensive Ni and Co resources in conventional cathode materials. Al-doping can effectively suppress the Jahn-Teller effect of Mn^{3+} and enhance the electrochemical reversibility of $Mn^{4+/3+}$. Moreover, the P2-O2 phase transition is successfully suppressed by the incorporation of Al^{3+}, thus maintaining a capacity retention of 79.1% after 500 cycles at 2 C. Surprisingly, The ternary (Cu-Al-Mn) P2 phase cathode materials designed in this work exhibit excellent moisture stability, its crystal structure remains unchanged and maintains good electrochemical performance even after direct immersion in water for 6 h. DFT calculations reveal adsorption energy of the H_2O molecule increases from −2.98 eV to −1.35 eV after the incorporation of Al, indicating water molecules are more difficult to enter the interlayer of the P2 structure. The work provides a new idea for low-cost and moisture stable cathode material for large-scale sodium-ion batteries.

Declaration of competing interest

The authors declare that they have no known competing financial interests or personal relationships that could have appeared to influence the work reported in this paper.

CRediT authorship contribution statement

Xuan Wang: Writing – review & editing, Writing – original draft, Methodology, Investigation, Funding acquisition, Data curation. **Peng Sun:** Writing – review & editing, Validation, Formal analysis, Data curation. **Siteng Yuan:** Visualization, Validation, Investigation, Formal analysis. **Lu Yue:** Writing – review & editing, Project administration, Funding acquisition, Formal analysis. **Yufeng Zhao:** Writing – review & editing, Supervision, Project administration, Formal analysis, Conceptualization.

Acknowledgments

This work is supported by National Natural Science Youth Foundation of China (No. 22308294), National Natural Science Foundation of China (No. 22179077), Postgraduate Research & Practice Innovation Program of Jiangsu Province (No. SJCX23_1868), Qing Lan Project of Jiangsu University and the Funding for school-level research projects of Yancheng Institute of Technology.

Supplementary materials

Supplementary material associated with this article can be found, in the online version, at doi:10.1016/j.cclet.2024.110015.

References

[1] M. Armand, J.M. Tarascon, Nature 451 (2008) 652–657.
[2] Z. Yang, J. Zhang, M.C.W. Kintner-Meyer, et al., Chem. Rev. 111 (2011) 3577–3613.
[3] H. Liu, Z. Xu, B. Cao, et al., Adv. Energy Mater. 14 (2024) 2400318.
[4] M.D. Slater, D. Kim, E. Lee, C.S. Johnson, Adv. Funct. Mater. 23 (2013) 947–958.
[5] H. Pan, Y.S. Hu, L. Chen, Energy Environ. Sci. 6 (2013) 2338–2360.
[6] M. Han, J. Liu, C. Deng, et al., Adv. Energy Mater. 14 (2024) 2400246.
[7] J.Y. Hwang, S.T. Myung, Y.K. Sun, Chem. Soc. Rev. 46 (2017) 3529–3614.
[8] H. Liu, Z. Xin, B. Cao, et al., Adv. Energy Mater. 34 (2024) 2309840.
[9] C. Delmas, C. Fouassier, P. Hagenmuller, Phys. B+C 99 (1980) 81–85.
[10] Z. Lum, J.R. Dahn, J. Electrochem. Soc. 148 (2001) 1225.
[11] D. Tie, G. Gao, F. Xia, et al., ACS Appl. Mater. Interfaces 11 (2019) 6978–6985.
[12] X. Bai, M. Sathiya, B. Mendoza-Sánchez, et al., Adv. Energy Mater. 8 (2018) 1802379.
[13] X. Wang, X. Yin, X. Feng, et al., Chem. Eng. J. 428 (2022) 130990.
[14] D. Sehrawat, S. Cheong, A. Rawal, et al., CrystEngComm 21 (2019) 172–181.
[15] Y. Fang, L. Xiao, Z. Chen, et al., Electrochem. Energy Rev. 1 (2018) 294–323.
[16] B. Namkoong, N.Y. Park, G.T. Park, et al., Adv. Energy Mater. 12 (2022) 2200615.
[17] Y. Li, Z. Yang, S. Xu, et al., Adv. Sci. 2 (2015) 1500031.
[18] S.Y. Xu, X.Y. Wu, Y.M. Li, Y.S. Hu, L.Q. Chen, Chin. Phys. B 23 (2014) 118202.
[19] Z. Lu, J.R. Dahn, Chem. Mater. 13 (2001) 1252–1257.
[20] Z.Y. Li, X. Ma, K. Sun, et al., ACS Appl. Energy Mater. 5 (2022) 1126–1135.
[21] M.S. Kwon, S.G. Lim, Y. Park, et al., ACS Appl. Mater. Interfaces 9 (2017) 14758–14768.
[22] U. Garg, W. Rexhausen, N. Smith, et al., J. Power Sources 431 (2019) 105–113.
[23] C. Cheng, M. Ding, T. Yan, et al., Small Methods 6 (2022) 2101524.
[24] X. Liu, W. Zuo, B. Zheng, et al., Angew. Chem. Int. Ed. 58 (2019) 18086–18095.
[25] H. Jo, S.Y. Song, E. Cho, et al., Inorg. Chem. 56 (2017) 9369–9375.
[26] Z. Xiao, F. Xia, L. Xu, et al., Adv. Funct. Mater. 32 (2022) 2108244.
[27] L. Wang, Y.G. Sun, L.L. Hu, et al., J. Mater. Chem. A 5 (2017) 8752–8761.
[28] S. Gu, H. Wang, C. Wu, et al., Energy Storage Mater. 6 (2017) 9–17.
[29] E. Talaie, V. Duffort, H.L. Smith, B. Fultz, L.F. Nazar, Energy Environ. Sci. 8 (2015) 2512–2523.
[30] H. Nara, K. Morita, D. Mukoyama, et al., Electrochim. Acta 241 (2017) 323–330.
[31] Y. Xiao, N.M. Abbasi, Y.F. Zhu, et al., Adv. Funct. Mater. 30 (2020) 2001334.
[32] Q. Liu, Z. Wu, J. Sun, et al., Electrochim. Acta 437 (2023) 141473.
[33] W.L. Pang, X.H. Zhang, J.Z. Guo, et al., J. Power Sources 356 (2017) 80–88.
[34] Y. Qi, Y. Lu, F. Ding, et al., Angew. Chem. Int. Ed. 58 (2019) 4361–4365.
[35] T. Jin, P.F. Wang, Q.C. Wang, et al., Angew. Chem. Int. Ed. 59 (2020) 14511–14516.
[36] H. Kim, H. Kim, Z. Ding, et al., Adv. Energy Mater. 6 (2016) 1600943.
[37] D. Dai, X. Lai, X. Wang, et al., Chin. Chem. Lett. 35 (2024) 109405.
[38] Y.H. Jung, A.S. Christiansen, R.E. Johnsen, P. Norby, D.K. Kim, Adv. Funct. Mater. 25 (2015) 3227–3237.
[39] X. Zhou, Y. Huang, B. Wen, et al., Proc. Natl. Acad. Sci. U. S. A. 121 (2024) 2316914121.
[40] P. Wang, Y. You, Y. Yin, Y. Guo, Adv. Energy Mater. 8 (2018) 1701912.
[41] W. Zuo, J. Qiu, X. Liu, et al., Energy Storage Mater. 26 (2020) 503–512.
[42] B. Cao, S. Gao, Y. Ma, et al., J. Colloid Interface Sci. 661 (2024) 598–605.
[43] J.Y. Hwang, J. Kim, T.Y. Yu, Y.K. Sun, Adv. Energy Mater. 9 (2019) 1803346.
[44] R. Chen, D.S. Butenko, S. Li, et al., Chin. Chem. Lett. 35 (2024) 108358.
[45] L. Zheng, J. Li, M.N. Obrovac, Chem. Mater. 29 (2017) 1623–1631.
[46] Y. Wang, W. Li, G. Hu, et al., Chem. Mater. 31 (2019) 5214–5223.
[47] M. Han, Z. Zou, J. Liu, et al., Small 20 (2024) 2312119.
[48] X. Chen, X. Zhou, M. Hu, et al., J. Mater. Chem. A 3 (2015) 20708–20714.
[49] P.F. Wang, Y. You, Y.X. Yin, et al., Angew. Chem. Int. Ed. 55 (2016) 7445–7449.
[50] Z. Lu, J.R. Dahn, J. Electrochem. Soc. 148 (2001) A710.
[51] C. Karra, P. Venkatachalam, K.K. Duru, et al., J. Electrochem. Soc. 168 (2021) 050509.
[52] T.R. Chen, T. Sheng, Z.G. Wu, et al., ACS Appl. Mater. Interfaces 10 (2018) 10147–10156.
[53] P.F. Wang, Y. You, Y.X. Yin, Y.G. Guo, Adv. Energy Mater. 8 (2018) 1701912.
[54] Q. Shi, R. Qi, X. Feng, et al., Nat. Commun. 13 (2022) 3205.
[55] D. Buchholz, L.G. Chagas, C. Vaalma, L. Wu, S. Passerini, J. Mater. Chem. A 2 (2014) 13415–13421.
[56] Z. Liu, J. Shen, S. Feng, et al., Angew. Chem. Int. Ed. 60 (2021) 20960–20969.
[57] Y. Zhang, M. Wu, W. Teng, et al., ACS Appl. Mater. Interfaces 12 (2020) 15220–15227.
[58] S. Yuan, L. Yu, G. Qian, et al., Nano Lett. 23 (2023) 1743–1751.